Title

Direct measurement of local oxygen concentration in the bone marrow of live animals.

Journal

Nature, 508(7495)

ISSN

0028-0836

Authors

Spencer, Joel A
Ferraro, Francesca
Roussakis, Emmanuel
et al.

Publication Date

2014-04-01

DOI

10.1038/nature13034

Peer reviewed

HHS Public Access

Author manuscript

Nature. Author manuscript; available in PMC 2014 October 10.

Published in final edited form as:

Nature. 2014 April 10; 508(7495): 269–273. doi:10.1038/nature13034.

Direct measurement of local oxygen concentration in the bone marrow of live animals

Joel A. Spencer[1,2], **Francesca Ferraro**[3,4,5], **Emmanuel Roussakis**[1], **Alyssa Klein**[3,4,5], **Juwell Wu**[1,2], **Judith M. Runnels**[1,2], **Walid Zaher**[1,2], **Luke J. Mortensen**[1,2], **Clemens Alt**[1,2], **Raphaël Turcotte**[1,2,6], **Rushdia Yusuf**[3,4,5], **Daniel Côté**[7], **Sergei A. Vinogradov**[8], **David T. Scadden**[3,4,5], and **Charles P. Lin**[1,2,4,*]

[1]Wellman Center for Photomedicine, Massachusetts General Hospital, Harvard Medical School, Boston, Massachusetts, USA

[2]Center for Systems Biology, Massachusetts General Hospital, Harvard Medical School, Boston, Massachusetts, USA

[3]Center for Regenerative Medicine, Massachusetts General Hospital, Harvard Medical School, Boston, MA, USA

[4]Harvard Stem Cell Institute, Cambridge, MA, USA

[5]Department of Stem Cell and Regenerative Biology, Harvard University, Cambridge, MA, USA

[6]Department of Biomedical Engineering, Boston University, Boston, MA, USA

[7]Département de Physique, Génie Physique et Optique and Centre de Recherche de l'Institut Universitaire en Santé Mentale de Québec, Université Laval, Québec City, Québec G1J 2G3, Canada

[8]Department of Biochemistry and Biophysics, University of Pennsylvania, Philadelphia, PA, USA

Abstract

Characterizing how the microenvironment, or niche, regulates stem cell activity is central to understanding stem cell biology and to developing strategies for therapeutic manipulation of stem cells[1]. Low oxygen tension (hypoxia) is commonly thought to be a shared niche characteristic in maintaining quiescence in multiple stem cell types[2–4]. However, support for the existence of a hypoxic niche has largely come from indirect evidence such as proteomic analysis[5], expression of HIF-1 and related genes[6], and staining with surrogate hypoxic markers (e.g. pimonidazole)[6–8].

*Correspondence and requests for materials should be addressed to Dr. Charles P. Lin (charles_lin@hms.harvard.edu).

Author Contributions

J.A.S. designed and built the microscope, designed experiments, conducted research, collected and analyzed data and wrote the manuscript; F.F. designed experiments, conducted research, collected and analyzed data, and wrote the manuscript; E.R. synthesized the PtP-C343 oxygen probe; A.K. helped conduct research and collected and analyzed data; J.W., J.M.R., W.Z., L.J.M., R.T., and R.Y. helped conduct research; C.A. and D.C. helped build the microscope; S.A.V. synthesized the PtP-C343 oxygen probe and wrote the manuscript; D.T.S. designed experiments and wrote the manuscript; C.P.L. designed experiments, sponsored the project, and wrote the manuscript.

Author Information

The authors declare no competing financial interests. Reprints and permissions information is available at www.nature.com/reprints.

Here we perform direct *in vivo* measurements of local oxygen tension (pO_2) in the bone marrow (BM) of live mice. Using two-photon phosphorescence lifetime microscopy (2PLM), we determined the absolute pO_2 of the BM to be quite low (<32 mmHg) despite very high vascular density. We further uncovered heterogeneities in local pO_2, with the lowest pO_2 (~9.9 mmHg, or 1.3%) found in deeper peri-sinusoidal regions. The endosteal region, by contrast, is *less* hypoxic as it is perfused with small arteries that are often positive for the marker *nestin*. These pO_2 values change dramatically after radiation and chemotherapy, pointing to the role of stress in altering the stem cell metabolic microenvironment.

The precise location of a hematopoietic stem cell (HSC) niche within the BM remains elusive, with evidence supporting the existence of both a vascular niche[9,10] and an endosteal niche[11,12]. As the BM is densely perfused[13–16], including the endosteal region, we ask how such a highly vascularized tissue can harbor HSCs in a low oxygen microenvironment. The possibility of very steep pO_2 gradients forming hypoxic zones at short distances away from the blood vessels is suggested by an *in silico* model[17,18]. However no direct measurement of local oxygen distribution within the BM has been reported.

Here we implemented 2PLM on a two-photon microscope designed specifically for live animal imaging[19]. The all-optical design (**Extended Data** Fig. 1) enabled non-contact pO_2 measurement through the intact skull at precise locations within the BM with micrometer spatial resolution. Prior to imaging, a metalloporphyrin-based two-photon-enhanced phosphorescent probe PtP-C343[20,21] was injected systemically. The emissive triplet state of the platinum porphyrin (PtP) is highly sensitive to local oxygen concentration[20,21]. Bimolecular collisions with dissolved oxygen shorten the probe's triplet lifetime and quench phosphorescence[22]. Thus by measuring the phosphorescence decay time τ after an excitation pulse, the absolute pO_2 value can be determined based on a pre-established τ vs. pO_2 calibration curve (**Extended Data** Fig. 2). The metalloporphyrin in PtP-C343 is protected by a dendrimer with a polyethylene glycol (PEG) overcoat (**Extended Data** Fig. 3) to insure biocompatibility and to prevent unwanted interactions of the probe with bio-macromolecules[20,23]. To enhance the two-photon excitation cross section, several coumarin-343 (C343) moieties are grafted onto the dendrimer shell as two-photon "antennas" that funnel the captured energy to the metalloporphyrin by way of intramolecular energy transfer[20,21].

The residual fluorescence of the coumarin units in the probe enabled visualization of the BM vasculature by conventional two-photon excited fluorescence, while the bone was visualized simultaneously by the collagen second harmonic generation (SHG) signal[14]. We confirmed that the BM contains high vascular density (Fig. 1a–c), with > 95% of voxels in the image stack located < 25 μm from the nearest blood vessel (Fig 1b–c). We then quantified BM pO_2 at multiple intravascular locations using 2PLM and obtained values that ranged from 11.7 to 31.7 mmHg (1.5–4.2%) with a mean of 20.4 mmHg (2.7%). These values are significantly lower than the pO_2 in the microvasculature of the brain[24–26], the periosteum, and the cortical bone (Fig. 1d). In many instances we were able to follow individual blood vessels as they penetrated from the bone into the BM cavity (Fig. 1e). When traced along individual vessels, we detected steep drops in pO_2, measured immediately before and after entrance into the

BM cavity (Fig. 1e–f). The rapid depletion of oxygen along the direction of blood flow, where the blood transits from a region of low cellularity (cortical bone) to a region of high cellularity (BM), is reminiscent of the *longitudinal* pO_2 gradient observed when blood vessels enter solid tumors with high metabolic demand[27].

Because of the relatively high permeability of the BM vasculature, the injected probe (diameter ~3–4 nm)[20] diffused out of the blood vessels and accumulated in sufficient concentrations within minutes (**Extended Data** Fig. 4) to allow pO_2 measurements in the interstitial space. In accordance with the mathematical models[17,18], we found a steep *lateral* pO_2 gradient away from the blood vessels, with a mean extravascular pO_2 of 13.3 mmHg (1.8%) and a range of 4.8 to 21.1 mmHg (0.6–2.8%) (Fig. 1d).

Our measured pO_2 in the BM (~20.4 mmHg intravascular, ~13.3 mmHg extravascular) agreed well with a previously reported value of ~18 mmHg obtained using an oxygen electrode[7]. That measurement, however, lacked spatial resolution, and the insertion of the needle electrode most likely damaged the microvasculature so that only an averaged reading of intravascular and extravascular pO_2 was recorded. Nevertheless, taken together these results support the notion that the BM as a whole is a hypoxic tissue despite its high vascularity.

To provide a finer grained view of oxygen distribution within the BM, we noted that the vasculature is heterogeneous, with smaller vessels located closer to the endosteal surface (Fig. 2a). 2PLM of blood vessels with diameters < 15 μm shows higher pO_2 (22.7 mmHg, 3.0%) than blood vessels with diameters > 15 μm (19.5 mmHg, 2.6%, $p < 0.03$). Accordingly, when we analyzed the pO_2 values at different distances from the endosteum, we found the lowest pO_2 to be in the regions > 40 μm from the bone, with values of 17.7 mmHg (2.4%) in the vessels and 9.9 mmHg (1.3%) outside the vessels (Fig. 2a). In the endosteal region (0–20 μm zone) where most of the smaller vessels are located, the pO_2 readings were slightly higher, with values of 21.9 mmHg (2.9%, $p < 0.03$) in the vessels and 13.5 mmHg (1.8%, $p < 0.01$) outside the vessels (Fig. 2a). These measurements uncovered a moderate pO_2 gradient with distance from the endosteum, but the direction of the gradient was unexpected. Instead of the endosteal zone being the most hypoxic, we found that the pO_2 decreased with increasing distance away from the endosteum toward the more hypoxic sinusoidal region.

As there are currently no HSC-specific markers for visualizing the endogenous stem cells under homeostatic conditions, we used the nestin-GFP mouse to help identify the locations where HSCs reside. Nestin is expressed by a subset of BM mesenchymal stem cells (MSCs) that are involved in HSC maintenance and trafficking[9], and perivascular nestin-GFP bright cells define a quiescent HSC niche[16]. We reasoned that if hypoxia regulates quiescence[5], then nestin-GFP cells should be a landmark for hypoxic regions in the BM. In nestin-GFP mice, we confirmed that nestin+ cells are predominantly perivascular, and transplanted HSCs home close to nestin+ vessels (**Extended Data Fig. 5)**[9]. Nestin+ vessels are anatomically distinct from nestin- vessels, being located closer to the bone surface (10.9 μm vs. 25.5 μm, $p < 0.02$) and much smaller in diameter (9.5 μm vs. 22.9 μm, $p < 2\times10^{-6}$) (Fig.

2b). Contrary to our expectation, we found the pO_2 to be significantly higher in nestin+ compared to nestin- vessels (22.8 mmHg vs. 17.6 mmHg, $p < 0.0007$) (Fig. 2c–d).

Next we examined whether transplanted hematopoietic stem/progenitor cells (HSPCs) home to BM niches with distinct pO_2 levels. Prior to transplantation, recipient animals were given cytoreductive conditioning with either radiation or chemotherapy (busulfan, 35 mg/kg). Remarkably, both treatments resulted in a substantial elevation in the overall BM pO_2 (Fig. 3a). The rise in pO_2 was striking considering that the vasculature was severely damaged after both radiation and chemotherapy (**Extended Data Fig. 6a–c**). Moreover, while the intravascular pO_2 values were essentially unchanged after sub-lethal irradiation (4.5 Gy), the gradient between intravascular and extravascular pO_2 disappeared, with the extravascular pO_2 rising to the same level as the intravascular pO_2 (Fig. 3a). The “negative” gradient of decreasing pO_2 with increasing distance away from the endosteum also disappeared (Fig. 3b). In the case of lethal irradiation and busulfan treatment, the extensive vascular damage caused such widespread dye leakage that the boundary between intravascular and extravascular spaces could no longer be delineated.

We performed HSPC transplantation (~10^5 lineage-cKit+Sca1+ (LKS) cells per recipient) 24 hours after busulfan treatment and measured the pO_2 around each LKS cell that homed to the calvarial BM 18–24 hours later. We obtained pO_2 values that span nearly the entire range of the (elevated) BM pO_2 in the post-chemotherapy setting (Fig. 3c), indicating that HSPCs did not seek out specific niches defined by low pO_2 as sites for preferential homing.

These observations compelled us to reexamine blood flow in the BM[28]. Specifically we asked whether the differences in pO_2 observed in nestin+ vs. nestin- vessels and in steady-state vs. radiation/chemotherapy treated animals could be accounted for, at least in part, by the blood flow profiles. We injected CFSE-labeled red blood cells (RBCs) and increased our imaging speed to 120 frames per second (scanning ¼ of the frame size) to enable tracking of individual RBC flow direction and speed. Interestingly, the highest RBC flow velocities are observed in nestin+ vessels (> 2 mm/sec, compared to 0.2–1 mm/sec in sinusoidal vessels). The vascular network map shows that the nestin+ vessels are always upstream of and drain into sinusoidal vessels (Fig. 4a), suggesting that nestin+ vessels have arterial characteristics. *In vivo* immunostaining[29] with fluorescent anti-Sca-1 antibody confirms they are arteries[15](**Extended Data Fig. 7a**).

Flow imaging with labeled RBCs also helps to overcome the dye leakage problem after radiation/chemotherapy and enables us to delineate the functional blood vessels by analyzing the tracks of the flowing RBCs in the video sequence. We found a surprisingly robust flow 2–6 days after lethal irradiation (**Extended Data Fig. 7b and Extended Data Video 1),** a time when the BM cellularity is declining precipitously (**Extended Data Fig. 8**). A combination of ample blood supply and reduced oxygen consumption (reduced BM cellularity) can explain the elevation of the pO_2 after radiation and chemotherapy. The reduced BM cellularity can also explain why the gradient between intra- and extra-vascular pO_2 disappears after the myelosuppressive conditioning.

To further establish the link between cellularity and oxygen consumption, we infused 25×10^6 total marrow cells from GFP donor mice into lethally irradiated DsRed recipients (Fig. 4b). We verified by FACS on day 2 and 5 that most of the proliferating (Ki-67+) cells are in the donor fraction (Fig. 4c). Then, by *in vivo* imaging, we showed that the bone marrow contained heterogeneous patches of donor (GFP+) and recipient (DsRed+) cells, with corresponding differences in local pO_2 (Fig. 4b). Lower pO_2 was associated with large clusters of green cells, consistent with the notion that the proliferating cells consume oxygen more avidly (Fig. 4d).

In summary, direct measurements of the absolute pO_2 in the BM has revealed a unique hypoxic landscape organized by its dense vascularity (oxygen supply) and high cellularity (consumption). The balance between supply and consumption can be altered by stress such as radiation and chemotherapy. The local topography is further defined by the positioning of different types of blood vessels within the BM (**Extended Data Fig. 9**). In particular, HSCs near nestin+ arteries and those near sinusoidal vessels will experience different metabolic milieus, highlighting the need to further examine the role of distinct vascular niches in HSC regulation.

Methods

Two-photon pO_2 microscope

The microscope is composed of two excitation arms: a video-rate laser-scanning two-photon imaging arm and a point-detection two-photon phosphorescence lifetime sensing arm (**Extended Data** Fig. 1). Output from a 80 MHz femtosecond laser source (MaiTai, Newport, Mountain View, CA) tuned to 840 or 913 nm is split into s- and p-polarizations by a polarizing beamsplitter (PBS1). The s-polarized beam passes through PBS1 and enters the imaging arm whereas the p-polarized beam is deflected 90° into the point detection arm. The power for each arm can be adjusted by rotating a half-wave plate in front of PBS1. These polarized beams are later recombined by a second polarizing beamsplitter (PBS2) immediately before entering the objective.

For the point-detection arm, the beam is swept across a slit aperture (NT38-560, Edmund Optics) using a galvanometric scanner (6220H, Cambridge Technology) and imaged onto the sample to form a ~3.5 μm scan line. Such one-dimensional scanning simultaneously served two purposes. First, it generated an excitation gate with adjustable pulse duration (15–40 μsec), determined by the scanning speed across the slit aperture. Secondly, it served to reduce the triplet state saturation effects that may accompany stationary excitation[30], thus helping to prevent degradation of the point spread function in the axial dimension. After application of the excitation gate, the arrival time of individual phosphorescence photons was recorded using a custom photon counting circuit. The histogram of the photon arrival times was then analyzed to obtain the triplet state lifetime. We found that the standard deviation of the pO_2 measurement was typically under 4 mmHg and inversely proportional to the signal-to-noise ratio (SNR, data not shown).

For the imaging arm, we use a similar scan engine as described previously and combine the beam with the point-detection arm using PBS2[19]. The beam is then focused by a 60× 1.2 NA

water immersion, infinity corrected, near-infrared coated objective (UPLSAPO 60XW, Olympus America Inc.) with a working distance of 280 μm.

Description and Calibration of PtP-C343

The two-photon antenna, coumarin 343, within PtP-C343 (**Extended Data** Fig. 3) has a two-photon absorption cross section (σ_2) of ~28 GM at 840 nm and a fluorescent quantum yield φ_{fl}) of ~0.90[20]. This means that the two-photon action cross-section ($\eta = \sigma_2\varphi_{fl}$) of PtP-C343 is ~25.2 GM. The FRET efficiency (ϕ_{FRET}) of C343 and PtP is ~0.68[20]. The phosphorescence lifetime of PtP-C343 in the absence of oxygen (τ_0) is ~60 μs[20] with a dynamic range well suited for the physiological range of pO_2. For calibration, we recorded lifetime measurements in a pH 7.4 buffered solution of PtP-C343 at 38° C *in vitro* over a range of pO_2 recorded independently by an oxygen electrode (OX-500, Unisense A/S, **Extended Data** Fig. 2). Our results match a published curve for the same batch of dye (**Extended Data** Fig. 2).

Animal Preparation

All procedures were approved by the Institutional Animal Care and Use Committee (IACUC) at Massachusetts General Hospital. Male wild-type C57BL/6J (Jackson Laboratory) and C57BL/6 Nes-GFP mice < 6 months of age were used for all *in vivo* PtP-C343 experiments[31]. In a typical experiment, anesthesia was slowly induced in mice via inhalation of a mixture of 1.35–2% isoflurane and O_2. To maintain anesthesia the mixture was reduced to 1.25% isoflurane with 98.75% O_2. This protocol minimizes the effect of anesthesia on tissue pO_2[32]. Calvarial bone was exposed through a U-incision in the scalp to create a skin flap and 2% methocellulose gel was placed on the scalp for refractive index matching.

The mouse then received an intravenous injection of 100–180 μl of 1.7 mM PtP-C343 suspended in 0.9% phosphate buffered saline (1x PBS, Invitrogen) and 40–60 μl of 10 mg/ml 70 kDa RhodamineB-Dextran (Life Technologies Corporation). We used relatively high amounts of PtP-C343 in order to accomplish a sufficient concentration outside of the blood vessels for interstitial measurement of pO_2. The mouse was placed on a heated stage with the skull positioned under the objective as described previously[29]. An approximately 4×6 mm area of the calvarium encompassing most of the parasagittal BM cavities within the left and right frontal bones was scanned in each imaging session and appropriate locations were selected for pO_2 measurements. In agreement with previous *in vivo* studies[24–26], no apparent toxicity or phototoxicity was observed using the PtP-C343 probe. After imaging, the scalp was closed with 6-0 sutures and the mouse allowed to wake up. For terminal experiments, the mice were either sacrificed by dislodgement of the spinal cord or by euthanasia with CO_2.

When analyzing vessel size as a function of distance to the endosteal surface, we noticed that vessels 20–40 μm and > 40 μm away from the bone surface were generally larger than the 0–20 μm zone with average diameters of 27.0 and 26.9 μm, respectively ($p < 0.002$ and 0.06, respectively, Fig. 2a). The region > 40 μm away from the bone surface constituted a

dense network of sinusoidal vessels, which were more irregular in shape compared to vessels near the bone surface (Fig. 2a).

For cytoreductive conditioning, mice were conditioned on Day 0 with either irradiation (4.5 Gy or 9.5 Gy) or chemotherapy (busulfan, 35 mg/kg) and imaged on Day 2. For HSPC transplantation, ~10^5 FACS sorted HSPCs (lin-/c-kit+/Sca1+) were stained with Cell-Tracker Green (Life Technologies Corporation) and injected intravenously on Day 1.

For whole BM transplantation, four-month old male C57BL/6J mice (Jackson Laboratory, Bar Harbor, ME) or male actin-DsRed knock-in mice (Cg-Tg(CAG-DsRedMSTNagy/J, Jackson Laboratory, Bar Harbor, ME) were lethally irradiated with a single dose of 9.5 Gy gamma irradiation from a Cs137 source (Gammacel Exactor, Nordion, Ottawa, CA) 4 hours before rescue with 25×10^6 whole bone marrow cells from a donor actin-GFP knock-in mouse (C57BL/6-Tg(CAG-EGFP)131Osb/LeySopJ, Jackson Laboratory, Bar Harbor, ME).

On the fifth day following irradiation and transplantation, the actin-DsRed recipient mice were imaged and pO_2 measurements acquired in the BM. C57BL/6J mice were sacrificed, femurs and tibias extracted, and the marrow prepared for analysis of cycling cells. RBCs were lysed on ice using Red Blood Cell Lysing Buffer (Sigma Chemical Co., St. Louis, MO). The remaining bone marrow cell fraction was counted, fixed, permeabilized and stained with PE-conjugated Ki-67 according to the manufacturer's recommendations (BD Pharmingen/Biosciences, San Diego, CA). Analysis of cycling cells was performed on a SORP FACSAria II instrument (BD Biosciences, San Diego, CA).

For vascular mapping, we extracted blood from a donor C57BL/6 mouse, isolated the RBCs, labeled 7×10^6 RBCs with CFDA-SE (Life Technologies Corporation) @ 15 μM for 12 min @ 37° C (labeling concentration ~20×10^6 RBC/mL, in PBS without Ca + 0.2% bovine serum albumin + 0.2 g/L glucose), and washed 2x. We then suspended the RBCs in 200 μL of 400 nMQtracker 655 (Life Technologies Corporation) vascular label-PBS solution or 200 μL of 3 mg/ml 70 kDa RhodamineB-Dextran vascular label-PBS solution and intravenously injected the solution into the donor Nes-GFP mice immediately prior to imaging.

For *in vivo* anti-Sca-1 staining, we first demonstrated the *in vivo* specificity of the anti-Sca-1 antibody. We intravenously injected 20 μg of Trustainfcx (BioLegend catalog #B164564) into a C57BL/6J mouse to block non-specific Fc binding. Two hours later, we intravenously injected ~15 μg of PE-Cy7 anti-Sca-1 antibody (BD Biosciences catalog #108114) and ~15 μg of PerCP-Cy5.5 Rat IgG2a isotype control antibody (eBioscience catalog #45-4321-80). We then imaged the BM 24 hours later and found that anti-Sca-1 antibody had high specificity compared to the isotype control (data not shown). We then repeated the same protocol in a Nes-GFP mouse.

Image quantification

Using the axial-stacks, the distance of each pO_2 measurement to the nearest bone surface (endosteum) was computed as described previously[14]. Briefly, the shortest distance to the endosteum was determined in three dimensions using the Pythagorean Theorem. The vessel diameter was measured using the Rhodamine B dextran signal. This measurement was only

performed in the x-y plane and is the diameter of the lumen of the vessel. Both the distance and vessel diameter measurements were performed in ImageJ v. 1.47p. For display purposes, the brightness and contrast of Figure 1a–b, 1e, 4a–b, Extended Data Figures 4, 6, and 7, and Extended Data Video 1 were adjusted. All image analysis was performed on raw images. In Figure 1a, the maximum intensity projection image displayed only includes ~23 μm of depth in the blue channel. We did not include the full thickness for the blue channel because the bone SHG signal covers over the majority of the image at the most shallow depths.

For distance measurements to blood vessels, 3D stacks were re-sliced using Fiji (Image JA v. 1.45b) into the vertical planes (Y-Z, X-Z) and digitally rotated to remove the tilt of the skull relative to the imaging plane. Subsequently, for each R/G/B channel, the grayscale intensity profile along the Z direction was measured and fitted into an empirical exponential decay curve, the inverse of which was then multiplied to each stack image to equalize the image intensity as a function of depth. Next, the 3D stack was converted into binary images and manually verified for structural accuracy. Applying the Exact Euclidean Distance Transform (EEDT) function on the binarized red (blood vessel) channel stack returned the 3D distance of each non-vascular pixel to the nearest blood vessel wall as a 32-bit grayscale image stack. Pixels outside the bone marrow space were excluded using binarized blue (bone) channel stack. A histogram of EEDT distances hence described the distribution of distances from each pixel in the intra-marrow, non-vascular space to its nearest blood vessel.

Signal-to-noise ratio and statistical analysis

The signal-to-noise ratio (SNR) of the pO_2 measurements was calculated using the following formula:

$$\mathrm{SNR}=\mathrm{n}/\sqrt{(\mathrm{n}+2*\mathrm{n}_{\mathrm{BD}})},$$

where n is the number of photon counts and n_{BD} is the background count determined using the background value described above. n_{BD} is the combined signal from dark counts and background from stray light with the majority arising from dark counts. Phosphorescent measurements with a SNR below 20 were excluded from this study.

Sample size required for the experiments was estimated based upon results of preliminary data. All p-values were determined using a two-tailed, unequal variance Student's T Test except for Fig. 1f and 4c where a two-tailed, paired Students's T Test and a one-tailed, paired Student's T Test were used, respectively. For cases where multiple statistical tests were performed on the same data set, statistical significance was determined using the Bonferroni correction. No blinding or randomization was performed for any of the experiments.

Acknowledgments

We thank Dr. Sava Sakadzic for helpful discussion on setting up the 2PLM experiment. This work was supported by the US National Institutes of Health grant HL097748, EB017274 (to CPL), HL097794, HL096372 and EB014703 (to DTS).

References

1. Lymperi S, Ferraro F, Scadden DT. The HSC niche concept has turned 31. Annals of the New York Academy of Sciences. 2010; 1192:12–18. [PubMed: 20392212]
2. Suda T, Takubo K, Semenza GL. Metabolic regulation of hematopoietic stem cells in the hypoxic niche. Cell Stem Cell. 2011
3. Mohyeldin A, Garzón-Muvdi T, Quiñones-Hinojosa A. Oxygen in stem cell biology: a critical component of the stem cell niche. Cell Stem Cell. 2010
4. Lee KE, Simon MC. From stem cells to cancer stem cells: HIF takes the stage. Current opinion in cell biology. 2012
5. Unwin RD. Quantitative proteomics reveals posttranslational control as a regulatory factor in primary hematopoietic stem cells. Blood. 2006; 107:4687–4694. [PubMed: 16507774]
6. Takubo K, Goda N, Yamada W, Iriuchishima H, Ikeda E. Regulation of the HIF-1α level is essential for hematopoietic stem cells. Cell Stem Cell. 2010
7. Ceradini DJ, et al. Progenitor cell trafficking is regulated by hypoxic gradients through HIF-1 induction of SDF-1. Nat Med. 2004; 10:858–864. [PubMed: 15235597]
8. Parmar K, Mauch P, Vergilio JA, Sackstein R, Down JD. Distribution of hematopoietic stem cells in the bone marrow according to regional hypoxia. Proc Natl Acad Sci USA. 2007; 104:5431–5436. [PubMed: 17374716]
9. Méndez-Ferrer S, et al. Mesenchymal and haematopoietic stem cells form a unique bone marrow niche. Nature. 2010; 466:829–834. [PubMed: 20703299]
10. Kiel MJ, et al. SLAM family receptors distinguish hematopoietic stem and progenitor cells and reveal endothelial niches for stem cells. Cell. 2005; 121:1109–1121. [PubMed: 15989959]
11. Calvi LM, et al. Osteoblastic cells regulate the haematopoietic stem cell niche. Nature. 2003; 425:841–846. [PubMed: 14574413]
12. Wang LDL, Wagers AJA. Dynamic niches in the origination and differentiation of haematopoietic stem cells. Nat Rev Mol Cell Biol. 2011; 12:643–655. [PubMed: 21886187]
13. Lichtman MAM. The ultrastructure of the hemopoietic environment of the marrow: a review. Exp Hematol. 1981; 9:391–410. [PubMed: 7016565]
14. Celso, Lo C, et al. Live-animal tracking of individual haematopoietic stem/progenitor cells in their niche. Nature. 2009; 457:92–96. [PubMed: 19052546]
15. Nombela-Arrieta C, et al. Quantitative imaging of haematopoietic stem and progenitor cell localization and hypoxic status in the bone marrow microenvironment. Nat Cell Biol. 2013; 15:533–543. [PubMed: 23624405]
16. Kunisaki Y, et al. Arteriolar niches maintain haematopoietic stem cell quiescence. Nature. 2013; 502:637–643. [PubMed: 24107994]
17. Chow DC, Wenning LA, Miller WM, Papoutsakis ET. Modeling pO 2 Distributions in the Bone Marrow Hematopoietic Compartment. I. Krogh's Model. Biophys J. 2001
18. Chow DC, Wenning LA, Miller WM, Papoutsakis ET. Modeling pO 2 Distributions in the Bone Marrow Hematopoietic Compartment. II. Modified Kroghian Models. Biophys J. 2001
19. Veilleux I, Spencer JA, Biss DP, Cote D, Lin CP. In Vivo Cell Tracking With Video Rate Multimodality Laser Scanning Microscopy. Journal of Selected Topics in Quantum Electronics, IEEE. 2008; 14:10–18.
20. Lebedev AY, Troxler T, Vinogradov SA. Design of Metalloporphyrin-Based Dendritic Nanoprobes for Two-Photon Microscopy of Oxygen. J Porphyr Phthalocyanines. 2008; 12:1261–1269. [PubMed: 19763243]
21. Finikova OS, et al. Oxygen Microscopy by Two-Photon-Excited Phosphorescence. Chem Phys Chem. 2008; 9:1673–1679. [PubMed: 18663708]
22. Vanderkooi JMJ, Maniara GG, Green TJT, Wilson DFD. An optical method for measurement of dioxygen concentration based upon quenching of phosphorescence. J Biol Chem. 1987; 262:5476–5482. [PubMed: 3571219]
23. Lebedev AY, et al. Dendritic phosphorescent probes for oxygen imaging in biological systems. ACS Appl Mater Interfaces. 2009; 1:1292–1304. [PubMed: 20072726]

24. Sakadzić S, et al. Two-photon high-resolution measurement of partial pressure of oxygen in cerebral vasculature and tissue. Nat Methods. 2010; 7:755–759. [PubMed: 20693997]
25. Lecoq J, et al. Simultaneous two-photon imaging of oxygen and blood flow in deep cerebral vessels. Nat Med. 2011; 17:893–898. [PubMed: 21642977]
26. Kazmi SMS, et al. Three-dimensional mapping of oxygen tension in cortical arterioles before and after occlusion. Biomed Opt Express. 2013; 4:1061–1073. [PubMed: 23847732]
27. Dewhirst MWM, et al. Quantification of longitudinal tissue pO2 gradients in window chamber tumours: impact on tumour hypoxia. Br J Cancer. 1999; 79:1717–1722. [PubMed: 10206282]
28. Mazo IB, et al. Total body irradiation causes profound changes in endothelial traffic molecules for hematopoietic progenitor cell recruitment to bone marrow. Blood. 2002; 99:4182–4191. [PubMed: 12010824]
29. Sipkins DA, et al. In vivo imaging of specialized bone marrow endothelial microdomains for tumour engraftment. Nature. 2005; 435:969–973. [PubMed: 15959517]
30. Sinks LE, et al. Two-photon microscopy of oxygen: polymersomes as probe carrier vehicles. J Phys Chem B. 2010; 114:14373–14382. [PubMed: 20462225]
31. Mignone JL, Kukekov V, Chiang AS, Steindler D, Enikolopov G. Neural stem and progenitor cells in nestin-GFP transgenic mice. J Comp Neurol. 2004; 469:311–324. [PubMed: 14730584]
32. Esipova TV, et al. Two new ‘protected’ oxyphors for biological oximetry: properties and application in tumor imaging. Anal Chem. 2011; 83:8756–8765. [PubMed: 21961699]

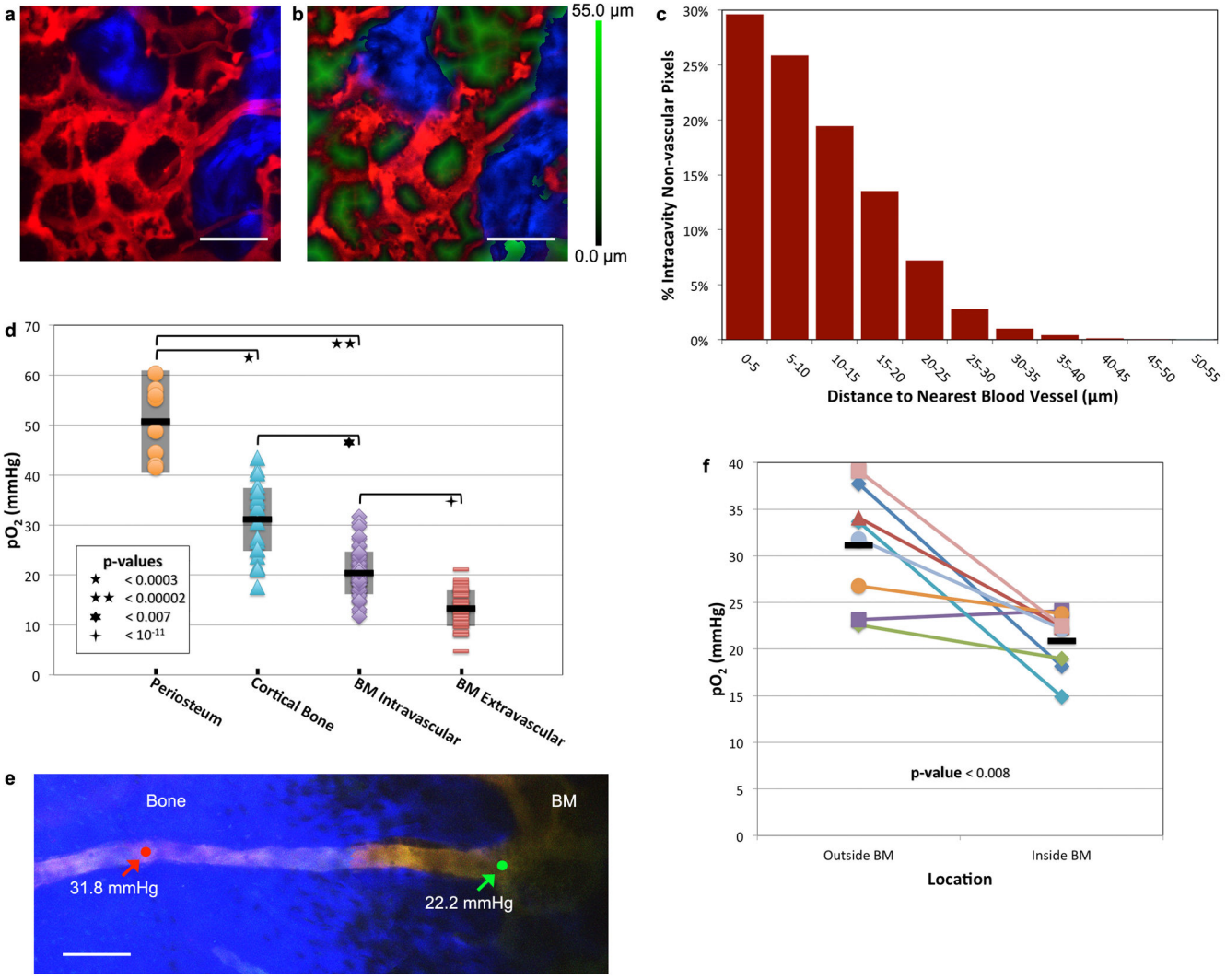

Figure 1. BM vascular density and oxygenation

(**a**) Intravital maximum intensity image (~75 µm thick) of mouse calvarial BM showing blood vessels (red, Qtracker 655 vascular dye) and bone (blue, collagen SHG). (**b**) Corresponding single plane of the 3D intravital imaging stack showing blood vessels (red), bone SHG (blue), and the 3D Euclidean distance measurement (EDM, green) to the nearest blood vessel wall for each extravascular pixel in the BM. (**c**) Histogram of all EDMs from the full 3D imaging stack. (**d**) BM pO_2 is significantly lower compared to pO_2 in periosteal and cortical bone vessels. Each point represents a pO_2 measurement in a separate blood vessel or interstitial position (n = 8, 21, 55, and 40 vessels/locations for periosteum, cortical bone, BM intravascular, and BM extravascular, respectively, from 8 mice). The mean (black line) and ± standard deviation (shaded box) for each data set is shown. (**e**) Maximum intensity projection image montage of a blood vessel entering the BM from the bone. Bone (blue) and blood vessels (yellow) are delineated with SHG and RhodamineB-dextran/PtP-C343 fluorescence, respectively. The two arrows point to locations of pO_2 measurements just before and after the vessel enters the BM. (**f**) Drop in pO_2 when tracking along

individual vessels upon entry into the BM (n = 8 vessels from 4 mice). The mean (black line) is shown for each data set. Scale bars ~100 μm.

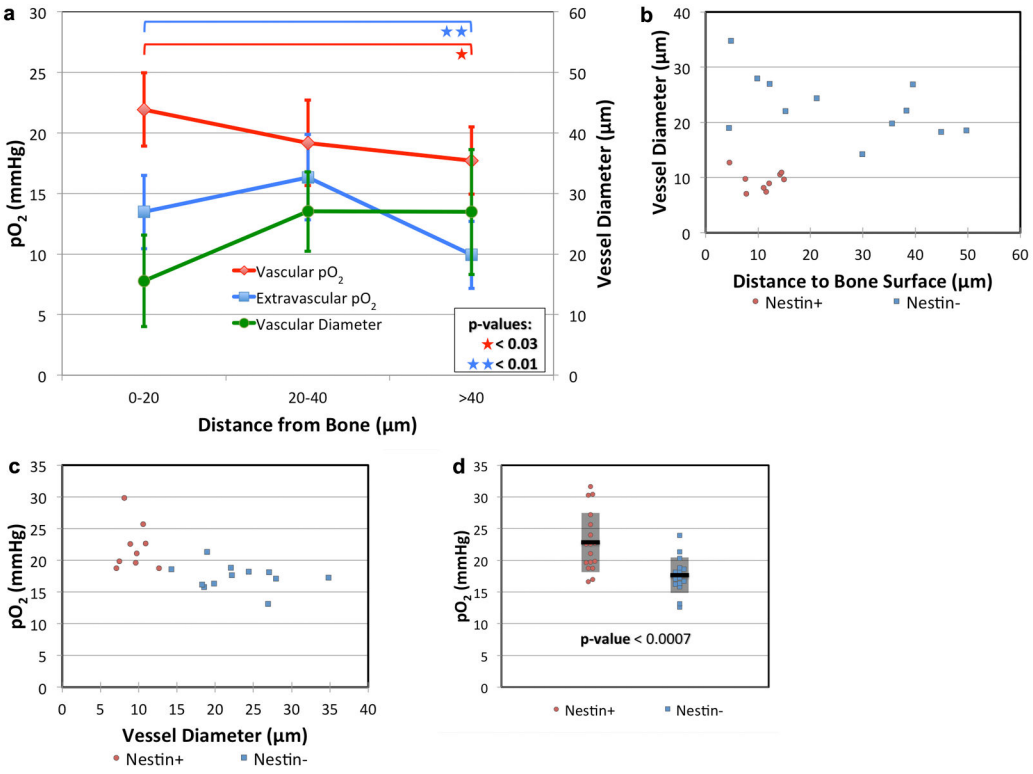

Figure 2. Variation in BM pO_2 according to vessel diameter and distance from the endosteal surface

(**a**) Average vessel diameter (green line, n = 38 vessels from 4 mice) and intravascular (red line, n = 38 vessels from 4 mice) and extravascular (blue line, n = 39 locations from 3 mice) pO_2 are plotted as a function of the distance from the bone surface to the measurement location. Error bars are the ± standard deviations. (**b**) The diameter of nestin+ (red circles, n = 9 vessels from 3 mice) and nestin- vessels (blue squares, n = 12 vessels from 3 mice) are plotted as a function of the distance from the endosteal surface. (**c**) The pO_2 of the same nestin+ and nestin- vessels are plotted as a function of vessel diameter. (**d**) Nestin+ (red circles, n = 17 vessels from 7 mice) and nestin- (blue squares, n = 16 vessels from 5 mice) vessel pO_2. The mean (black line) and ± standard deviation (shaded box) for each data set is shown.

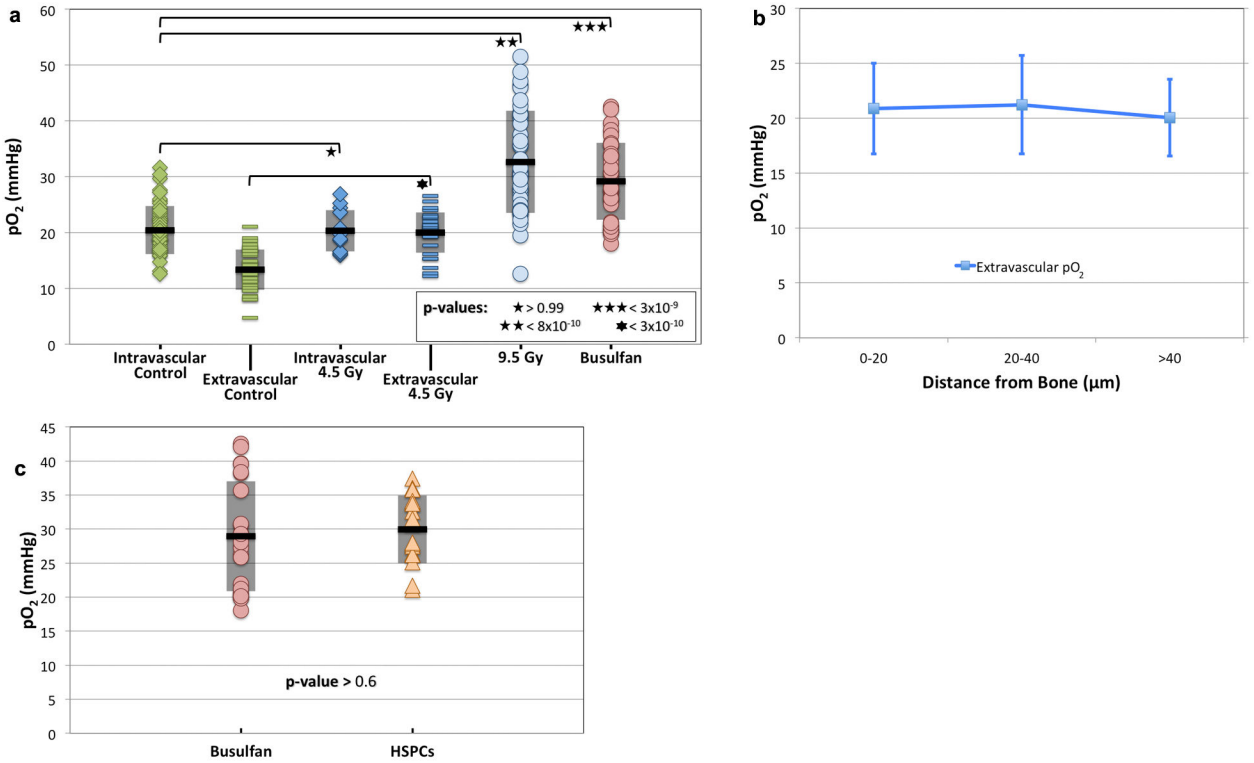

Figure 3. BM pO_2 after cytoreductive therapy and at sites of HSPC homing

(**a**) BM pO_2 two days after sublethal (4.5 Gy, n = 13 vessels and 29 extravascular locations from 5 mice) or lethal (9.5 Gy, n = 40 locations from 2 mice) gamma irradiation, or after busulfan (35 mg/kg, n = 40 locations from 6 mice) conditioning. The untreated control pO_2 from Figure 1d is plotted for comparison. (**b**) Extravascular pO_2 measurements are plotted as a function of distance to the bone surface from the measurement location 2 days after 4.5 Gy irradiation (n = 44 locations from 4 mice). (**c**) Comparison of pO_2 at sites of HSPC homing to the overall BM pO_2 in busulfan treated recipients (n = 17 HSPCs from 6 mice). No statistically significant difference was observed. For (**a**) and (**c**), the mean (black line) and ± standard deviation (shaded box) for each data set is shown.

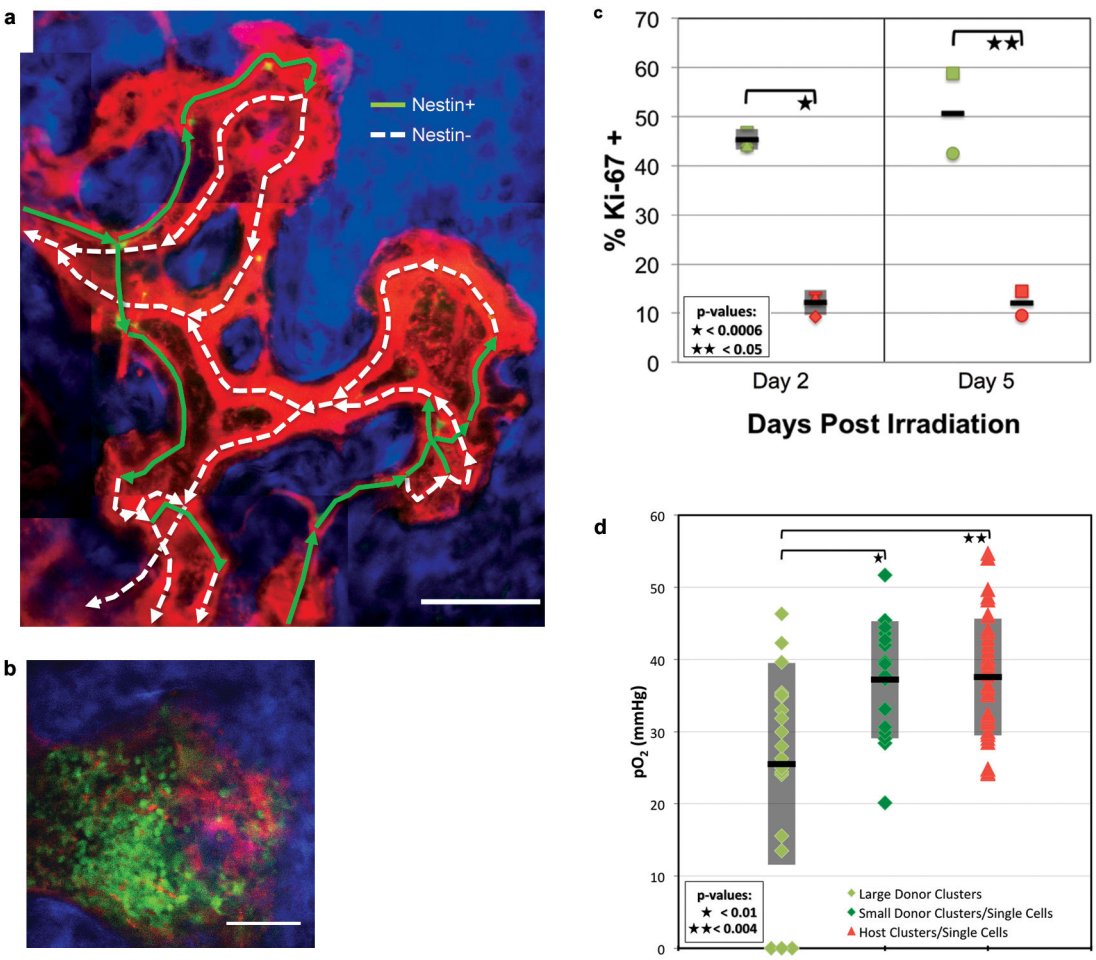

Figure 4. BM vascular mapping and the effects of cellularity on local pO_2 after cytoreductive conditioning

(**a**) Vascular connectivity map of a nestin-GFP mouse reveals that nestin+ vessels are upstream of and drain into sinusoids. Arrows indicating blood flow direction, determined by tracking the movement of labeled RBCs with video-rate imaging, are superimposed on a maximum intensity projection image of BM vasculature (red = vascular dye, green = nestin-GFP/RBCs, blue = SHG bone signal). A solid green line indicates a vessel with an adjacent nestin+ cell and a dashed white line indicates a nestin- vessel. Scale bar ~100 μm. (**b**) *In vivo* image of the bone marrow of a universal DsRed recipient 5 days after transplantation with 25 million total marrow cells from a universal GFP donor. Red = DsRed, Green = GFP, Blue = SHG from bone. Scale bar ~100 μm. (**c**) Ki-67 staining of green (donor) and red (host) BM cells by FACS on day 2 (n = 3 mice) and day 5 (n = 2 mice) after transplantation. Each symbol denotes a different mouse. Scale bars (day 2) are the ± standard deviation of the mean. (**d**) The *in vivo* pO_2 values in regions with large clusters of donor cells (n = 19 locations from 4 mice) compared to small donor clusters/single cells (n = 16 locations from 4 mice) and host clusters/single cells (n = 40 locations from 5 mice). The mean (black line) and ± standard deviation (shaded box) for each data set is shown.